



UNIVERSITY OF LEEDS

This is a repository copy of *A rapid one-step preparation method of the repairable three-dimensional antifouling superhydrophobic 2.5EPZF coating on magnesium alloys*.

White Rose Research Online URL for this paper:

<https://eprints.whiterose.ac.uk/205019/>

Version: Accepted Version

---

**Article:**

Xi, Z., He, X., Wu, Z. et al. (2 more authors) (2023) A rapid one-step preparation method of the repairable three-dimensional antifouling superhydrophobic 2.5EPZF coating on magnesium alloys. *Surfaces and Interfaces*, 42 (Part B). 103476. ISSN 2468-0230

<https://doi.org/10.1016/j.surfin.2023.103476>

---

**Reuse**

This article is distributed under the terms of the Creative Commons Attribution-NonCommercial-NoDerivs (CC BY-NC-ND) licence. This licence only allows you to download this work and share it with others as long as you credit the authors, but you can't change the article in any way or use it commercially. More information and the full terms of the licence here: <https://creativecommons.org/licenses/>

**Takedown**

If you consider content in White Rose Research Online to be in breach of UK law, please notify us by emailing [eprints@whiterose.ac.uk](mailto:eprints@whiterose.ac.uk) including the URL of the record and the reason for the withdrawal request.



[eprints@whiterose.ac.uk](mailto:eprints@whiterose.ac.uk)  
<https://eprints.whiterose.ac.uk/>

1 **A rapid one-step preparation method of the repairable three-dimensional**  
2 **antifouling superhydrophobic 2.5EPZF coating on magnesium alloys**

3 Zhongxian Xi<sup>a,b</sup>, Xiaoyan He<sup>a,b</sup>, Zumin Wu<sup>a,b</sup>, Chengqing Yuan<sup>a,b,\*</sup>, Chun Wang<sup>c</sup>

4 a Reliability Engineering and New Energy Institute, School of Transportation and Logistics  
5 Engineering, Wuhan University of Technology, Hubei, 430063, China

6 b National Engineering Research Center for Water Transport Safety, Wuhan University of  
7 Technology, Hubei, 430063, China

8 c Institute of Functional Surfaces, School of Mechanical Engineering, University of Leeds, Leeds  
9 LS2 9JT, United Kingdom

10 \*Corresponding author. *E-mail: ycq@whut.edu.cn (Chengqing Yuan)*

11 **Abstract:**

12 Although three-dimensional (3D) superhydrophobic coating has been gradually  
13 prepared on the surface of metal substrate for anticorrosion and antifouling, their  
14 complex preparation steps and equipment requirements limit their practical application.  
15 Herein, by a rapid one-step spray preparation method the fabricating 3D  
16 superhydrophobic 2.5EPZF (2.5 g epoxy resin/polycaprolactone (PCL)/zinc  
17 oxide/perfluorodecyltriethoxysilane) coating is prepared. This method utilizes a certain

18 degree of directional arrangement of macromolecular long chain polymers (PCL) as  
19 solvent evaporation during the spraying process to form a filamentous structure to  
20 construct the 3D coating. This preparation mechanism provides us a novel theoretical  
21 guidance method for preparing 3D coating. Further, the silk thickness and mesh  
22 density of the 3D mesh structure is controlled by adding epoxy resin. When the amount  
23 of epoxy resin is 2.5 g, the surface of 2.5EPZF coating is with about 1-3  $\mu\text{m}$  thick  
24 branch frame and 0.1-0.4  $\mu\text{m}$  thin treetop. And the water-contact angle (CA) of  
25 2.5EPZF is  $156.6 \pm 1.5^\circ$  and the sliding angle (SA) is  $< 10^\circ$ . The 2.5EPZF coating  
26 exhibits durable antifouling, strong mechanical&chemical durability, and corrosion  
27 resistance. The corrosion current of the 2.5EPZF coating for 0 day's immersion and 35  
28 days' immersion in NaCl solution is  $1.043 \times 10^{-12} \text{ A}\cdot\text{cm}^{-2}$  and  $1.1703 \times 10^{-11} \text{ A}\cdot\text{cm}^{-2}$ ,  
29 respectively. Under solar irradiation and at 50  $^\circ\text{C}$  for 30 min, the 2.5EPZF coating is  
30 with scratching recovering. Additionally, the composite coating can be prepared by a  
31 large area. It is expected that this method is readily used and shows great application  
32 potentials.

33 *Keywords:* PCL, Epoxy, Magnesium alloys, three-dimensional coating,  
34 superhydrophobic, anticorrosion and antifouling

35 **1. Introduction**

36 As a solar irradiation structural metal material, magnesium alloys have been widely  
37 used in automation industry, ship and automobile, aerospace, missile vehicle,  
38 electronic and electrical appliances, etc., due to its outstanding physical and  
39 mechanical properties, non-magnetic properties and good thermal dissipation [1-11]. In  
40 the field of marine automobile, magnesium alloys are used as instrument panel,  
41 steering wheel, gearbox, oil sump, gear box, cylinder cover, seat frame, deck and some  
42 wheel hubs, special vessels such as small investigation and experiment ships use  
43 magnesium alloys as the hull shell structure and so on [12-18]. However, the poor  
44 corrosion resistance of magnesium alloys, especially in the sea environment containing  
45 chloride ions, limits the application of magnesium alloys as solar irradiation weight  
46 materials for medium and large ships [19-22].

47 At present, the superhydrophobic coating prepared by one-step method usually was  
48 the two-dimensional (2D) coating, such as the epoxy resin  
49 (EP)/polymethylhydrosiloxane (PMHS)/modified nano-SiO<sub>2</sub> layer [23], the Maleic  
50 anhydride (MAH)/Epoxy resin grafted with fluorine containing side chains (FEP)  
51 coating [24], Epoxy resin (EP)/Polydimethylsiloxane (PDMS)/SiO<sub>2</sub> coating [25], and

52 so on. The stability of the superhydrophobic coating maintains the continuous air film  
53 to prevent the invasion of the corrosive media. Compared with 2D coating, the  
54 hydrophobic coating with three-dimensional (3D) micropore structure could anchor the  
55 air film more tightly in dynamic condition. The current creation of materials with 3D  
56 structures often adopts multi-step method (the preparation of fluffy ZnO rods/PDMS  
57 by spraying, hydrothermal method and modified by  
58 1H,1H,2H,2H-perfluorooctyltriethoxysilane [26]), sophisticated and special equipment,  
59 such as template method, foaming method, adding primary structural particles of  
60 specific shape (nanotube, filamentous, needle-shaped, four-corner needle-shaped, etc.),  
61 or adopting electrostatic spinning (the preparation of PCL/MSO/SiO<sub>2</sub> hierarchical  
62 superhydrophobic mats [27] and Polydimethylsiloxane (PDMS)-modified PCL  
63 membranes by electrospinning [28] ), 3D printing, optical or laser etching [29-32].  
64 These preparation methods are complicated in steps and long in cycle, or utilize special  
65 equipment with high requirements for electrospinning machines, 3D printers,  
66 lithography machines and other equipment, which is not convenient for large-area  
67 preparation, and is limited by the special structure and shape of the matrix, which is  
68 not conducive to large-scale promotion and application [30, 33, 34].

69 This work explores the use of the simple one-step spray method to generate  
70 three-dimensional reticulated porous 2.5EPZF composite coating on magnesium alloy  
71 substrate.

72 PCL, as a semi-crystalline non-toxic biodegradable polymer, is widely used in food  
73 packaging, drug release materials, biological implant materials and so on because of its  
74 certain hydrophobicity, excellent rheological properties and considerable toughness  
75 [22,35]. PCL can form three-dimensional reticulated and porous coating by spraying as  
76 a forming component. Epoxy resin (EP) is a thermosetting resin with excellent overall  
77 performance. It has good adhesion performance, outstanding corrosion resistance,  
78 excellent chemical resistance, low shrinkage characteristics, easy to process and low  
79 costs to be widely used in coating, adhesives and other fields [36-38]. Herein, the  
80 epoxy resin is as a molding control function, which can control the pore size and  
81 porosity of the three-dimensional network structure. Zinc oxide (ZnO) nanoparticles  
82 have the characteristics of safety, non-toxicity, high stability, strong photoelectric  
83 performance and good antibacterial activity, which are widely used in optoelectronic  
84 devices, environmental remediation, food packaging, coating rubber and other  
85 industries [39-41]. In this work, ZnO nanoparticles play an essential role in the

86 construction of micro-nano structure and the attachment of low-surface energy  
87 substances, improving the coating roughness and facilitating the uniform distribution  
88 of low-surface energy substances. 1H, 1H, 2H, 2H perfluorodecyltrichlorosilane  
89 (PFDTES) is a kind of fluorinated organic silane with low surface energy. In this paper,  
90 PFDTES is used to reduce the surface energy of materials, to improve the  
91 hydrophobicity and corrosion resistance of coating, and restrain the marine bacteria  
92 adhesion and fouling [42-45].

93 In this work, the superhydrophobic 2.5EPZF composite coating was prepared by  
94 one-step spraying method. The directional arrangement mechanization of  
95 macromolecular long chain polymers (PCL) as solvent evaporation during the spraying  
96 process to form a filamentous structure to construct provided a new preparation  
97 pathway to prepare the 3D coating. And this method could be used for large-scale 3D  
98 coating's preparation without the limitation of the substrate's shape.

## 99 **2. Experimental Section**

### 100 *2.1. Materials*

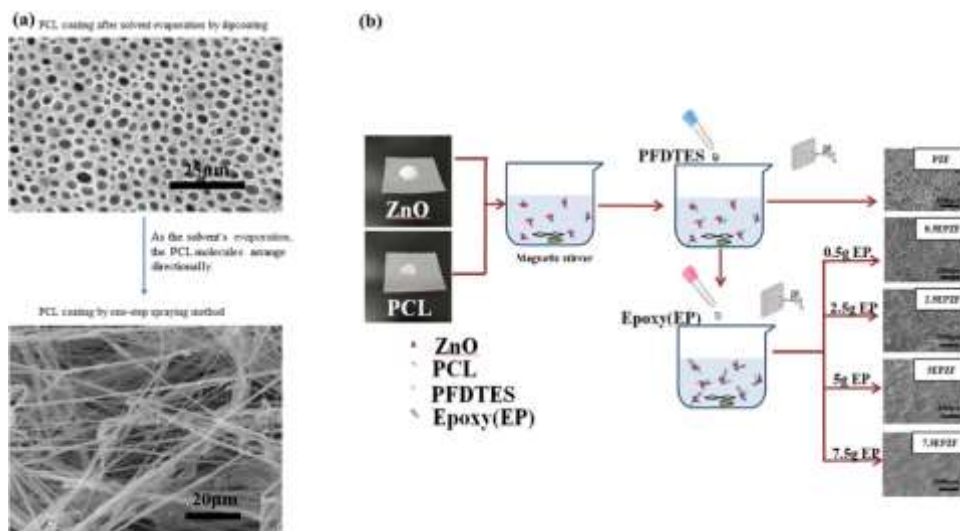
101 Dichloromethane (DCM) (Qingmei Chemical Reagent Factory, China),  
102 1H,1H,2H,2H-perfluorodecyltriethoxysilane (PFDTES) (Guangzhou Hongcheng

103 Biotechnology Science and Technology Co., LTD, China, 97%), PCL (Mw: 80,000,  
 104 Solvay Specialty Polymers, China), ZnO powders (30nm, Beijing Shenghehaoyuan  
 105 Tech. Co. Ltd., China) and Die-cast AZ91D magnesium alloy (Dongguan Qingmei  
 106 Metal Materials Co., Ltd., China) were used as the experimental materials. All  
 107 chemicals were used without further modification.

108 *2.2. Sample preparation*

109 Die-casted Mg alloy (AZ91D) with a chemical composition (wt.) of 8.77% Al, 0.74%  
 110 Zn, 0.18% Mn, 90.31% were cut into 50 mm x 25 mm x 5 mm. The samples were  
 111 polished by silicon carbide papers from 150 to 1000 mesh. Then the samples were  
 112 ultrasonically cleaned in acetone rinsed by de-ionized water, and dried at 60 °C for the  
 113 following coating preparation.

114 *2.3. Preparation of composite coating*



115

116 **Scheme 1.** The SEM of the PCL coating by dipcoating&spraying method (a) and the preparation process of the composite  
117 coating (b).

118 As shown in Scheme 1a, the PCL coating prepared by dipping would exhibit a  
119 regular multi-layer network structure in our former researches [46]. And we considered  
120 that the mechanism production of the regular network structure was the  
121 macromolecular long chain polymers (PCL) occurred a certain degree of directional  
122 arrangement during solvent evaporation. After multiple experiments, a  
123 three-dimensional network structure coating of PCL was prepared by simple spraying  
124 method as shown in Scheme 1a. By the same method, added ZnO nanoparticles (5 g,  
125  $6.14 \times 10^{-2}$  mol), PFDTES (1 mL,  $2.00 \times 10^{-3}$  mol) to the PCL solution (PCL 5g,  $6.25 \times$   
126  $10^{-5}$  mol, Dichloromethane (DCM, as the solvent), 80 mL) during the mixing process  
127 under vigorous stirring with a magnetic stirrer at RT as shown in Scheme 1b. Then,  
128 epoxy (EP) (0.5 g, 2.5 g, 5 g, 7.5 g) was added to the solution, respectively. The  
129 stirring process lasted for 1 hour. Then the polycaprolactone/epoxy resin/zinc  
130 oxide/perfluorodecyltriethoxysilane (EPZF) composite coating was prepared on the  
131 treated magnesium alloy substrate by one-step spray method under appropriate  
132 pressure with the stirred solution. After that, all samples were in the air at RT. for 24 h  
133 to dry and solidify. The PZF (polycaprolactone/zinc

oxide/perfluorodecyltriethoxysilane) coating was prepared by the same process as the control groups. The preparation conditions and the stirred solutions of samples with composite coating were shown in the table 1.

Sample	Stirred solutions	Preparation conditions
PZF	80 g DCM, 5 g PCL, 5 g ZnO, 1mL PFDTES	Room temperature
0.5EPZF	80 g DCM, 5 g PCL, 5 g ZnO, 1mL PFDTES, 0.5 g EP	45 s
2.5EPZF	80 g DCM, 5 g PCL, 5 g ZnO, 1mL PFDTES, 2.5 g EP	
5EPZF	80 g DCM, 5 g PCL, 5 g ZnO, 1mL PFDTES, 5 g EP	
7.5EPZF	80 g DCM, 5 g PCL, 5 g ZnO, 1mL PFDTES, 7.5 g EP	

**Table 1.** The preparation conditions and the stirred solution of samples with composite coating.

#### 2.4. Analysis of composite coating

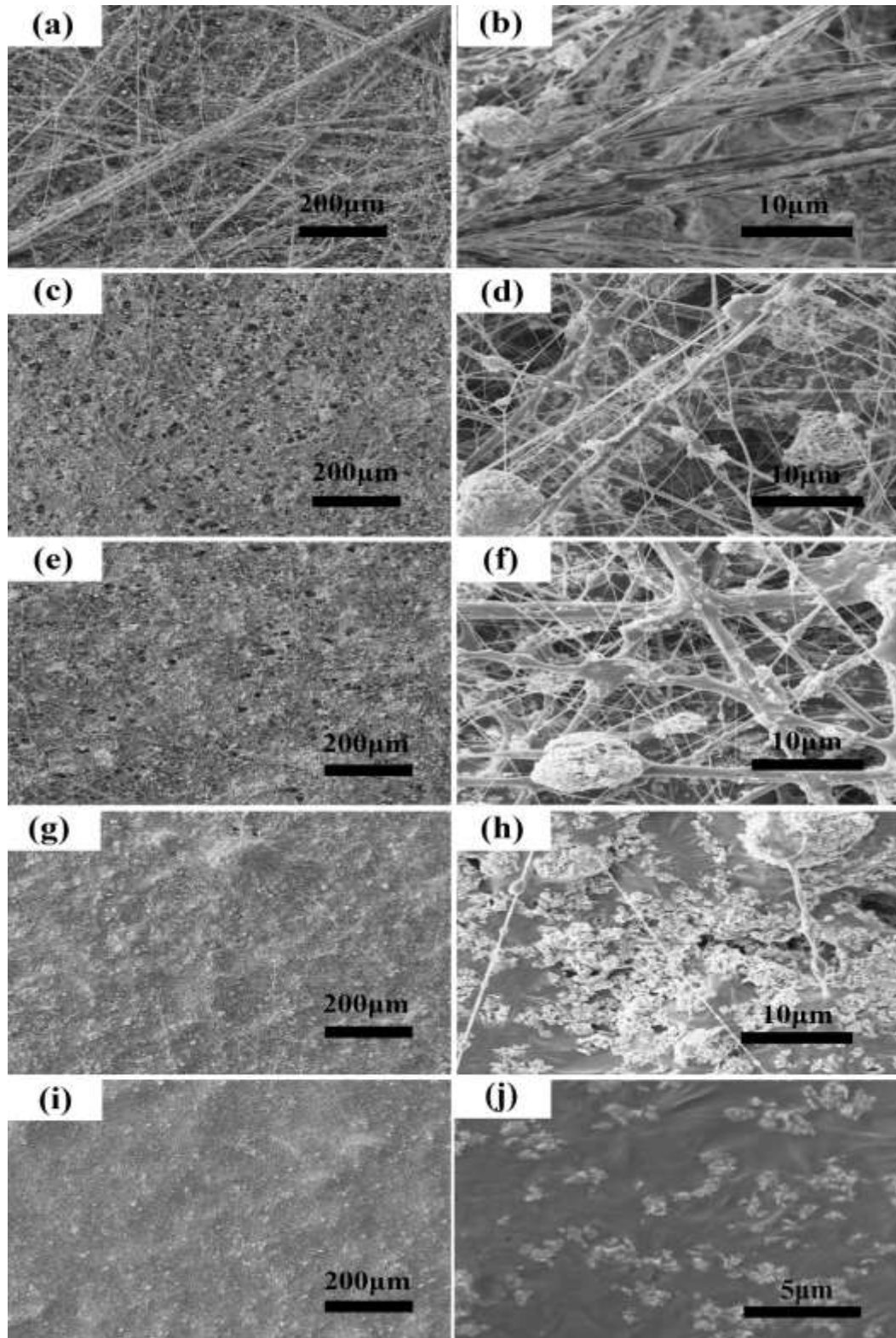
The surface morphology of the prepared coating was observed by using scanning electron microscopy (SEM, VEGA3, Tescan Co. China Ltd., China) equipped with energy-dispersive spectrometer (EDS). The water contact angle (CA) was measured at room temperature using an optical contact angle meter (Dataphysics OCA 15EC, Germany) with a 5  $\mu$ L water drop. Electrochemical tests were performed by electrochemical workstation (CorrTest CS350). The surface roughness of samples was measured by laser confocal microscope (CLSM) (VK-X1000, Keyence, Japan). The bacterial adhesion test was measured by using *Bacillus subtilis* CMCC (B) 63501 (Shanghai Luwei Technology Co., Ltd., China) at 120 rpm at 30 °C for 20 days. Subsequently, the samples were observed by SEM and digital camera to measure the *Bacillus* adhesion status and the surface corrosion resistance features. Then, the FTIR analysis of the coating was measured by Thermoscientific (Summit Pro, USA). Further, the samples' mechanical adhesion, self-cleaning ability, abrasion resistance and pH

152 durability, Bacillus subtilis adhesion and Solar irradiation&thermal repair were  
153 measured in our study. Three parallel samples were measured in the test progress.

### 154 **3. RESULTS AND DISCUSSION**

#### 155 *3.1. Surface characteristics*

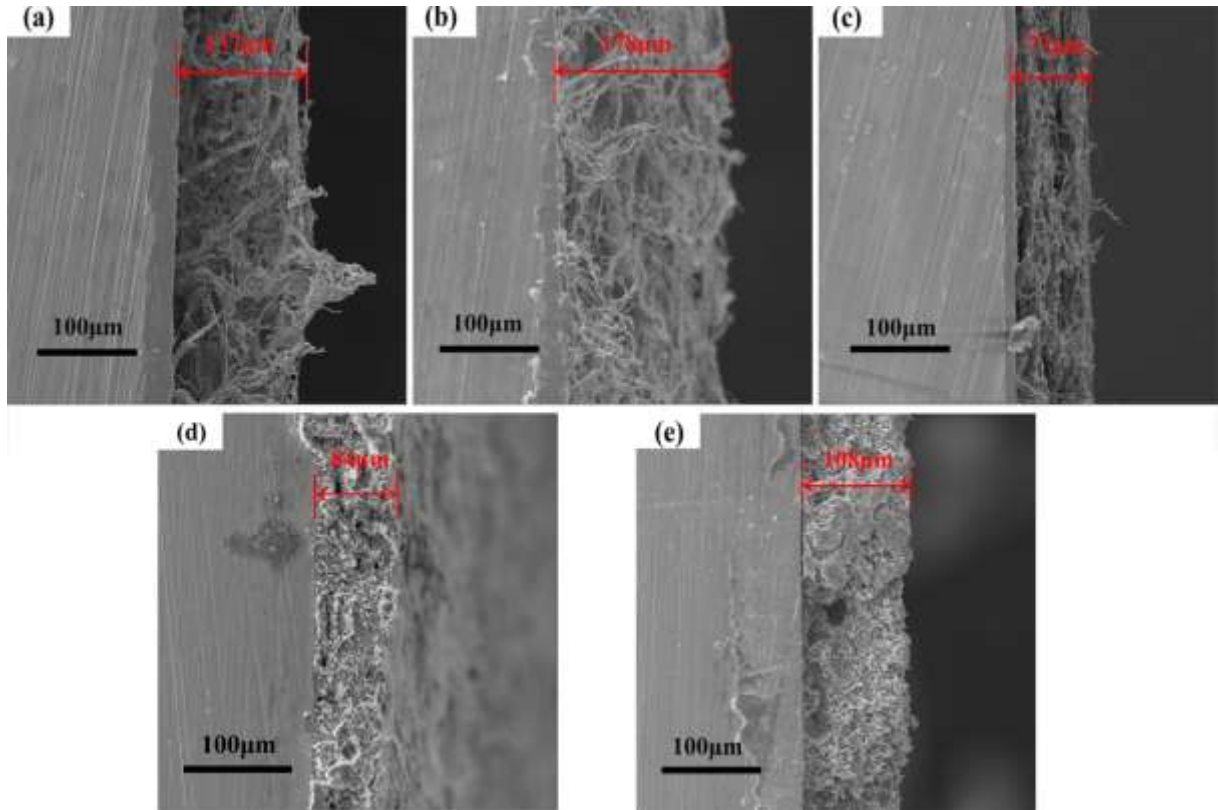
156 The SEM surface morphology of PZF, 0.5EPZF, 2.5EPZF, 5EPZF, 7.5EPZF  
157 samples was shown in Figure 1. The coating of PZF (Figure 1a and b) and 0.5EPZF  
158 (Figure 1c and d) exhibited a three-dimensional surface with network structure and  
159 high porosity. With the addition of 0.5 g epoxy resin, the samples were with lower  
160 porosity and the ZnO particles were dispersed in network structure. Then with the  
161 increase of epoxy resin content, the 2.5EPZF (Figure 1e and f) sample was with spatial  
162 wire mesh-like skeleton structure and lower porosity. The diameter of mesh and  
163 skeleton of 2.5EPZF sample were about 0.1-0.4  $\mu\text{m}$  and 1-3  $\mu\text{m}$ . After that, with more  
164 addition of epoxy resin content, the network and porous structure of the 5EPZF (Figure  
165 1g and h) and 7.5EPZF (Figure 1i and j) samples disappeared and the surface of  
166 7.5EPZF samples became smooth.



167 **Figure 1.** The SEM images of PZF (a and b), 0.5EPZF (c and d), 2.5EPZF (e and f), 5EPZF (g and  
 168 h), 7.5EPZF (i and j) samples.  
 169

170 The cross section SEM image of PZF (Figure 2a) and 0.5PZF (Figure 2b), 2.5EPZF  
 171 (Figure 2c), 5EPZF (Figure 2d), 7.5EPZF (Figure 2e) samples were shown in Figure 2.

172 The thickness of PZF (Figure 2a) and 0.5PZF (Figure 2b), 2.5EPZF (Figure 2c),  
173 5EPZF (Figure 2d), 7.5EPZF (Figure 2e) were about 137  $\mu\text{m}$ , 178  $\mu\text{m}$ , 77  $\mu\text{m}$ , 84  $\mu\text{m}$   
174 and 108  $\mu\text{m}$ , respectively. PZF and 0.5PZF samples were with three-dimensional  
175 network and porous structure. With the addition of 0.5 g EP, the coating thickness of  
176 0.5EPZF (Figure 2b) sample was with significant increase. It was because the support  
177 force of the filamentous structure between layers increased under 0.5 g addition of EP.  
178 With the continue adding of EP content, the coating thickness of 2.5EPZF sample  
179 became thinner markedly to 77  $\mu\text{m}$  (Figure 2c). And the reason was that the thin silk  
180 became thicker and the combination of filamentous structures between layers becomes  
181 tighter with 2.5 g EP addition. And then with the addition of 5 g EP and 7.5 g EP the  
182 thickness of composite coating gradually increased to 84  $\mu\text{m}$  (Figure 2d) and 108  $\mu\text{m}$   
183 (Figure 2e). With the addition of 5g and 7.5 g EP, the network and porous structure of  
184 the 5EPZF and 7.5EPZF samples almost disappeared. When the addition of 5 g and 7.5  
185 g EP could fully fill the pore, the thickness of the coating increased as the increasing  
186 amount of EP.



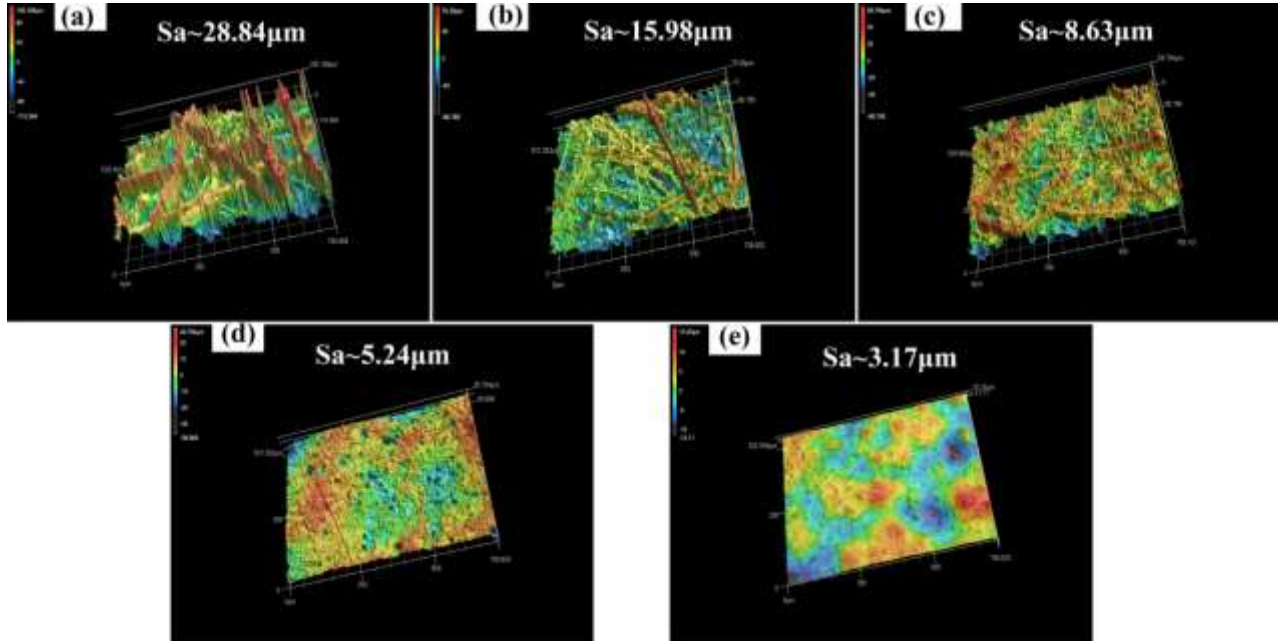
187  
188  
189

**Figure. 2.** The cross section SEM images of PZF (a) and 0.5EPZF (b), 2.5EPZF (c), 5EPZF (d), 7.5EPZF (e) samples.

### 190 3.2. Surface roughness characteristics

191 Moreover, roughness measurement with laser confocal microscope (VK-X1000,  
192 Keyence) and the 3D morphology of the samples of PZF (Figure 3a), 0.5PZF (Figure  
193 3b), 2.5EPZF (Figure 3c), 5EPZF (Figure 3d), 7.5EPZF (Figure 3e) samples was  
194 shown in Figure 3. The surface roughness of PZF (Figure 3a) and 0.5PZF (Figure 3b),  
195 2.5EPZF (Figure 3c), 5EPZF (Figure 3d), 7.5EPZF (Figure 3e) samples were 28.84  $\mu\text{m}$ ,  
196 15.98  $\mu\text{m}$ , 8.63  $\mu\text{m}$ , 5.24  $\mu\text{m}$  and 3.17  $\mu\text{m}$ . The change of coating roughness showed  
197 that the roughness of composite coating decreased obviously with the increase of  
198 epoxy resin content. When the amount of epoxy resin was 7.5 g, the 7.5EPZF

199 composite coating was almost flat which was consistent with the results observed in  
200 Figure 1i and j.

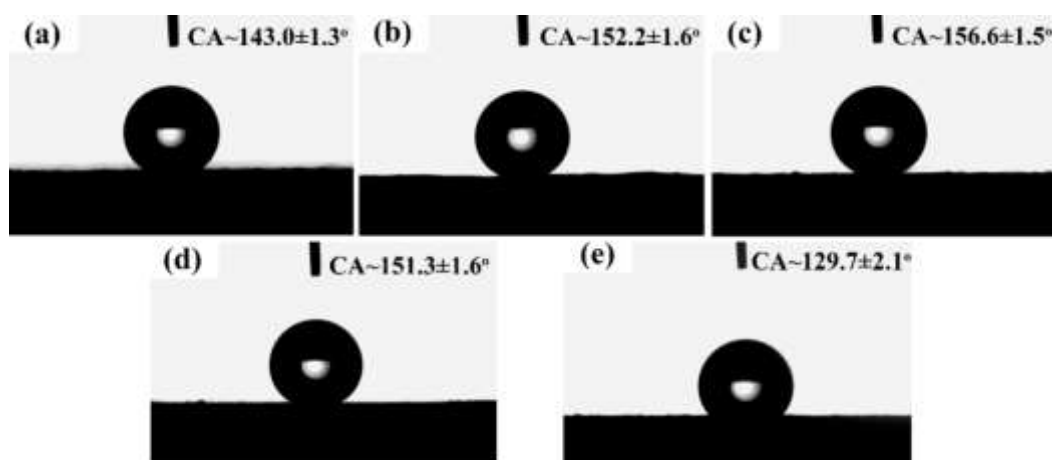


201  
202 **Figure 3.** The 3D morphology of the PZF (a) and 0.5PZF (b), 2.5EPZF (c), 5EPZF (d), 7.5EPZF (e) samples.

### 203 3.3. Wetting behaviors

204 The wettability of liquid droplets is an essential indicator to measure the protective  
205 properties of the coating. The hydrophobic performance can significantly prevent  
206 corrosive media and wetting, and prolong the service life of the coating. The contact  
207 angle (CA) of the coated samples was tested by the contact angle tester (Dataphysics  
208 OCA 15EC, Germany). The volume of the drops of deionized water was 5 $\mu$ l. The  
209 5-point measurements were tested for each sample. The contact angle test results of  
210 PZF, 0.5PZF, 2.5EPZF, 5EPZF, 7.5EPZF were shown in Figure 4.

211 In Figure 4a the contact angle test showed that the CA of the PZF composite  
212 coating was  $143 \pm 1.3^\circ$ . The PZF composite coating did not reach the  
213 superhydrophobicity ( $150^\circ$ ). As shown in Figure 1a and b, the reason was that the PZF  
214 coating was a loose porous structure and the excessive distance between the PZF silk  
215 made the hydrophobic air film discontinuous. With the increase of epoxy resin content,  
216 the contact angle began to increase. The CA of 0.5EPZF and 2.5EPZF composite  
217 coating were  $152.2 \pm 1.6^\circ$  (Figure 4b) and  $156.6 \pm 1.5^\circ$  (Figure 4c), respectively. And  
218 the SA of 2.5EPZF composite coating was  $< 10^\circ$ . As the amount of epoxy resin  
219 continued to increase, the CA of the composite coating decreased. The CA of the  
220 5EPZF composite coating and 7.5EPZF composite coating decreased to  $151.3 \pm 1.6^\circ$   
221 (Figure 4d) and  $129.7 \pm 2.1^\circ$  (Figure 4e), respectively. It illustrated that the composite  
222 coating changed from superhydrophobic to hydrophobic.



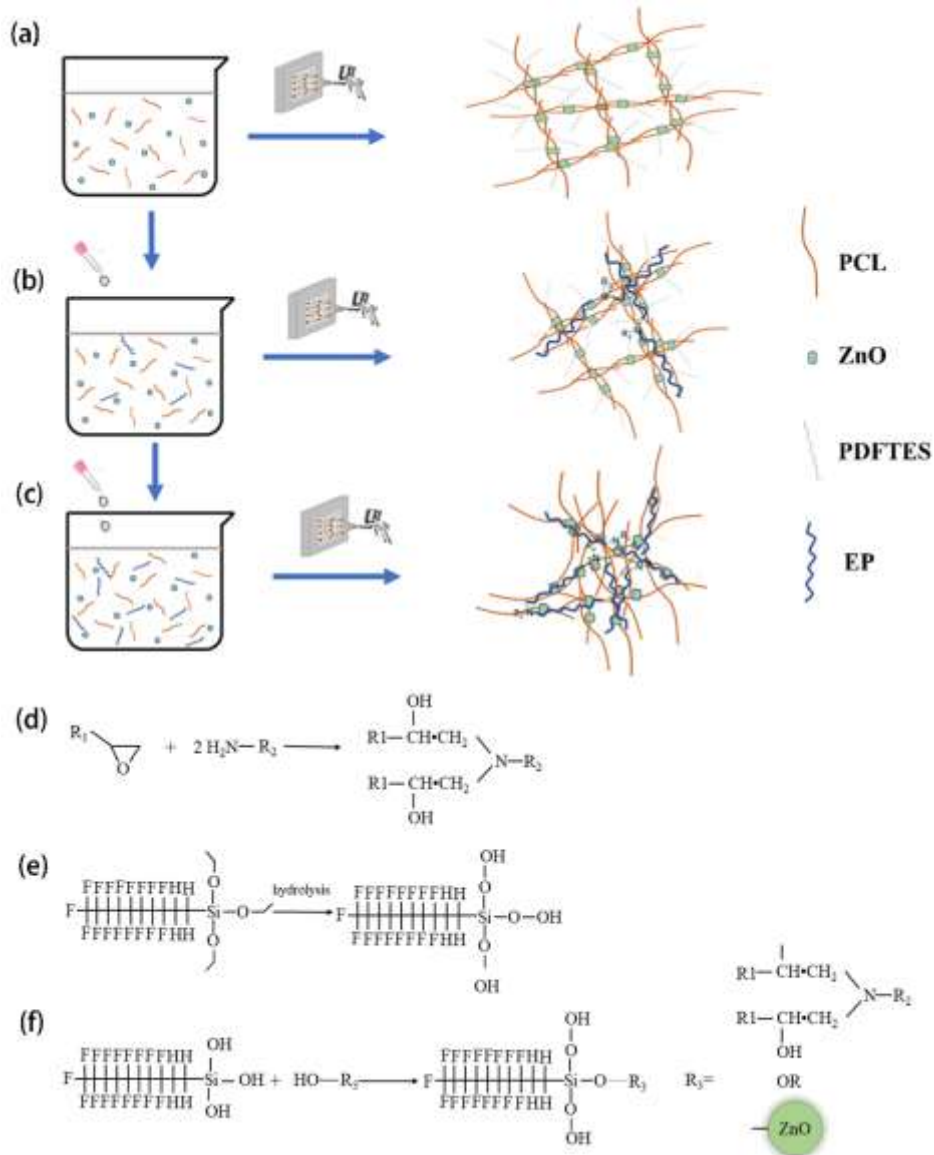
223 **Figure. 4.** The contact angle test results of PZF (a), 0.5EPZF (b), 2.5EPZF (c), 5EPZF (d) and 7.5EPZF (e)  
224 samples.  
225

226 3.4. Formation mechanism for the composite coating

227 The formation mechanism for the composite PZF and EPZF was shown in Figure 5.  
228 Without EP, the mixture of PCL, ZnO and PFDTES could form into the filamentous  
229 interweaving after the mixture spraying from the spray gun nozzle. It was because the  
230 PCL was a long chain macromolecules polymer with fewer branched chains. As the  
231 solvent evaporates, the PCL of the mixture would exhibit a certain directional  
232 arrangement to form a filamentous structure (Figure 5a). The curing mechanism of  
233 epoxy resin was shown in Figure 5d. After curing, epoxy resin was a long-chain high  
234 polymer with a three-dimensional configuration and the network structure of EP partly  
235 restricted the directional arrangement of long chain molecules (PCL) [39,40].

236 Additionally, the crosslinking of EP improves significantly as the amount of EP  
237 reagent added increases. As the addition amount of EP gradually increased, the coarse  
238 branch structure duly became thicker and more numerous (Figure 5b). When the  
239 addition amount of EP was 2.5 g, the composite coating was with a certain number of  
240 0.1-0.4  $\mu\text{m}$  filamentous structure and a significant amount 1-3  $\mu\text{m}$  coarse branch  
241 structure (Figure 1e and f, Figure 2c). Furtherore, with the addition amount of EP  
242 increased to 5 g and more, the crosslinking degree of epoxy resin continued to increase

243 and the filamentous structure&coarse branch structure vanished to form an overall  
 244 block structure coating (Figure 5c). Figure 5e was the hydrolysis of PFDTES [46]. The  
 245 hydrolysis product of PFDTES would combine with hydroxyl groups (ZnO and EP) to  
 246 form a modified surface (Figure 5f) [47, 48]. On the other side, due to the hydrophilic  
 247 group (-OH) of epoxy resin itself, when the amount of epoxy resin reached a certain  
 248 level, the composite coating became hydrophilic from hydrophobic.

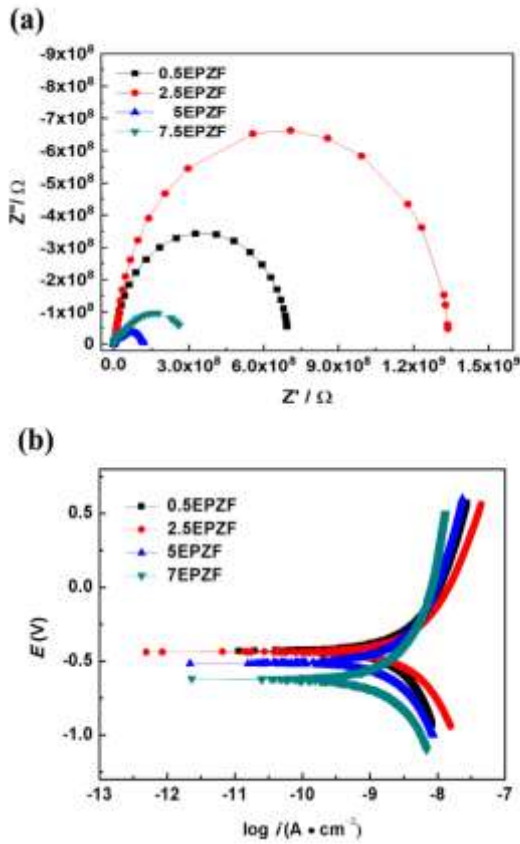


249  
 250

**Figure 5.** Formation mechanism for the composite coating of PZf and EPZf composite coating.

251 3.5. Electrochemical corrosion behavior

252 With a three-electrode system in 300 mL 3.5 wt.% NaCl electrochemical impedance  
253 spectra (EIS) were carried out [49]. Samples were exposed with a surface area of 1 cm<sup>2</sup>.  
254 A saturated calomel and a platinum mesh electrode were used as the reference and the  
255 counter electrode, respectively. At the open circuit potential (E<sub>corr</sub>), the scanning  
256 frequency range of electrochemical impedance test was 10<sup>5</sup>-10<sup>-2</sup> Hz, and the amplitude  
257 of sine wave disturbance was 10mV. The scanning rate of potentiodynamic polarization  
258 curve was 0.5 mV•s<sup>-1</sup>.



259 **Figure. 6.** EIS and potentiodynamic polarization results of EPZF composite coating with different amounts of  
260 epoxy resin.  
261

262 Figure 6 showed the EIS (a) and potentiodynamic polarization test results (b) of the  
 263 composite 0.5PZF, 2.5EPZF, 5EPZF, 7.5EPZF coating respectively. The size of  
 264 impedance arc could objectively reflect the corrosion performance of the coating. The  
 265 Nyquist diagram of EPZF composite coating with different amounts of epoxy resin was  
 266 shown in Figure 6a. With the addition of epoxy resin, the impedance arc was the  
 267 largest when the amount of epoxy resin is 2.5 g, about  $1.37 \times 10^9$ .

Samples	$I_{cor}$ (A/cm <sup>2</sup> )	$E_o$ (V)	Corrosion Rate (mm/a)
0.5EPZF	$6.2351 \times 10^{-10}$	-0.43216	$7.6118 \times 10^{-6}$
2.5EPZF	$1.043 \times 10^{-12}$	-0.43877	$1.2733 \times 10^{-8}$
5EPZF	$1.2716 \times 10^{-8}$	-0.7174	$1.5524 \times 10^{-4}$
7.5EPZF	$5.6863 \times 10^{-9}$	-0.6224	$6.9419 \times 10^{-5}$

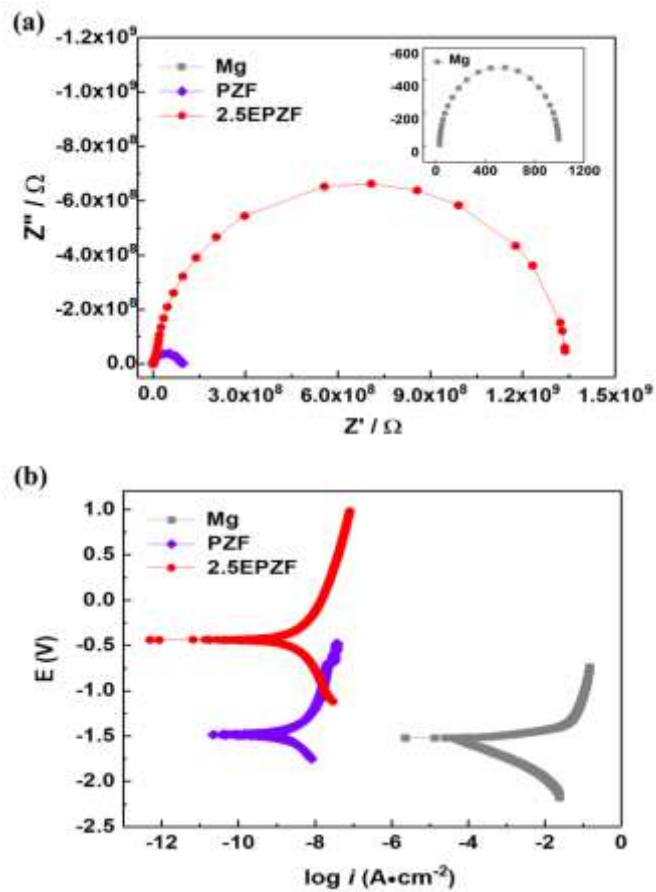
268 **Table 2.**  $E_{corr}$ ,  $i_{corr}$  and Corrosion Rate of the EPZF composite coating on Mg substrate with different amounts  
 269 of epoxy resin immersed in NaCl aqueous solutions (3.5 wt.%).

270 The electrochemical polarization test showed that with the increase of the amount  
 271 of epoxy resin, the corrosion current of the coating first decreased from  $6.2351 \times 10^{-10}$   
 272 A•cm<sup>-2</sup> (0.5EPZF) to  $1.043 \times 10^{-12}$  A•cm<sup>-2</sup> (2.5EPZF) with the addition of epoxy resin  
 273 from 0.5 g to 2.5 g. Then with the increase of epoxy resin content to 5.0 g, the  
 274 corrosion current enhanced while the corrosion performance diluted. It was because  
 275 with the raise of the amount of epoxy resin to 2.5 g, the network structure of the  
 276 coating became dense visibly, the porosity decreased significantly, and the proportion  
 277 of coarse branches increased. The dense pores tightly grasped the air to form a stable

278 air protection film, and this coating could reach the superhydrophobic state of  $156.6 \pm$   
279  $1.5^\circ$ , making the coating have good corrosion resistance. The thickness of 2.5EPZF  
280 composite coating was only  $77 \mu\text{m}$ . However, the 2.5EPZF composite coating had  
281 relatively best corrosion protection performance. When the amount of epoxy resin  
282 continued to increase to 5 g, the quality of porous structure was with a sharp decline.  
283 The contact angle test also showed that the hydrophobic property of the 5EPZF coating  
284 decreased demonstrably. The coating thickness of 5EPZF was  $95 \mu\text{m}$  which was thicker  
285 than 2.5EPZF, yet the corrosion rate of 5EPZF reduced by over 500 times. When epoxy  
286 resin addition was 7.5 g, the porous structure of the 7.5EPZF coating almost  
287 disappeared. At the same time, the 7.5EPZF coating was hydrophobic from  
288 superhydrophobic. The coating thickness of 7.5EPZF reached  $135 \mu\text{m}$ . It was about 1.6  
289 times the thickness of 2.5EPZF coating, but its corrosion resistance was worse than  
290 that of 2.5EPZF coating. It showed that the superhydrophobic three-dimensional  
291 porous structure of the thinner composite coating could greatly enhance the corrosion  
292 performance.

293 Here the 2.5EPZF sample was selected as the experiment sample, and magnesium  
294 alloy and PZF coating sample was used as the controlled sample for the following

295 electrochemical performance and adhesion test of marine bacterium (*Bacillus subtilis*).  
 296 Figure 7 showed the results of Nyquist impedance and potentiodynamic polarization  
 297 tests of uncoated magnesium alloy samples, the PZF coating sample and the 2.5EPZF  
 298 coating sample. EIS and potentiodynamic polarization results illustrated that the  
 299 2.5EPZF composite coating had the best corrosion resistance. And the corrosion  
 300 current of 2.5EPZF sample was  $1.043 \times 10^{-12} \text{ A}\cdot\text{cm}^{-2}$ .



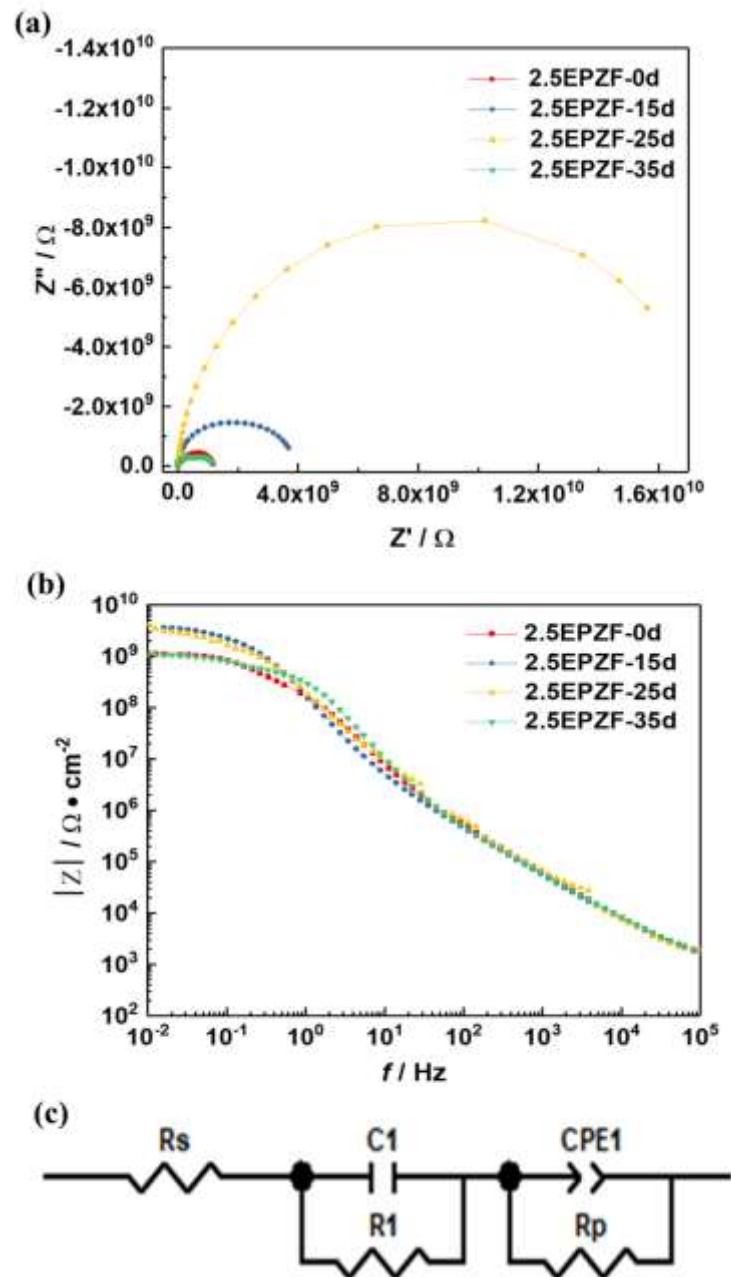
301  
 302 **Figure 7.** The Nyquist diagram and potentiodynamic polarization results of magnesium alloy substrate,  
 303 PZF and 2.5EPZF samples.

Samples	$I_{cor} (\text{A}/\text{cm}^{-2})$	$E_o (V)$	Corrosion Rate (mm/a)
Mg	$6.4746 \times 10^{-5}$	-1.5532	1.3951
PZF	$2.0373 \times 10^{-11}$	-1.0388	$0.5239 \times 10^{-7}$

2.5EPZF	$1.043 \times 10^{-12}$	-0.43877	$1.2733 \times 10^{-8}$
---------	-------------------------	----------	-------------------------

304 **Table 3.**  $E_{corr}$ ,  $i_{corr}$  and Corrosion Rate of the uncoated Mg substrate, PZF and 2.5EPZF composite coating  
 305 immersed in NaCl Aqueous Solutions (3.5 wt.%).

306 Further, the EIS of the 2.5EPZF sample was tested in NaCl Aqueous Solutions (3.5  
 307 wt.%) after different immersion times for 0 day, 15 days, 25 days, 35 days at  
 308 roomtemperature.



309

310 **Figure. 8.** Bode&Nyquist plots of 2.5EPZF composite coating at different immersion times in NaCl Aqueous  
311 Solutions (3.5 wt.%) and the corresponding equivalent electric circuit.

312 EIS of the 2.5EPZF sample in 3.5% NaCl solution for 35 days immersion was  
313 displayed in Figure 8. At the beginning, the Nyquist spectra present an arc with a large  
314 radius and the value of the low frequency impedance ( $|Z|_{0.01 \text{ Hz}}$ ) in Bode spectra is  
315 about  $1.37 \times 10^9 \Omega \cdot \text{cm}^{-2}$ , manifesting high barrier property of the coating to the  
316 substrate [50]. As shown in the Nyquist diagram (Figure 8a), for the 2.5EPZF coating,  
317 the impedance modulus cut from  $1.37 \times 10^9$  to  $3.90 \times 10^9 \Omega \cdot \text{cm}^{-2}$  severely after 15 days'  
318 immersion in NaCl Aqueous Solutions (3.5 wt.%). After 25 days' soaking, the  
319 impedance was increased to  $1.60 \times 10^{10} \Omega \cdot \text{cm}^{-2}$ . Under the pressure of the outside force  
320 (NaCl Aqueous Solutions), the deformation of treetop occurs and the pores of 2.5EPZF  
321 sample with mesh and skeleton coating become denser to grasp the air film firmly. It  
322 was caused by the diameter of mesh and skeleton of 2.5EPZF sample with about  
323 0.1-0.4  $\mu\text{m}$  Treetop structure and 1-3 $\mu\text{m}$  Branch structure. And the 1-3 $\mu\text{m}$  Branch  
324 structure of the 2.5EPZF coating provided the sufficient support to maintain the  
325 integrity of the air film. After 35 days' immersing, the impedance of 2.5EPZF sample  
326 was reduced to  $1.30 \times 10^8 \Omega \cdot \text{cm}^{-2}$ . During this time, the NaCl corrosion media  
327 gradually seeped into the surface of the air film with the measurably decrease of the

328 impedance modulus. Furthermore, the air film of 2.5EPZF coating was always present  
329 during 35 days' immersion. After 35 days' immersion, the corrosion current of the  
330 2.5EPZF coating was  $1.1703 \times 10^{-11} \text{ A}\cdot\text{cm}^{-2}$ .

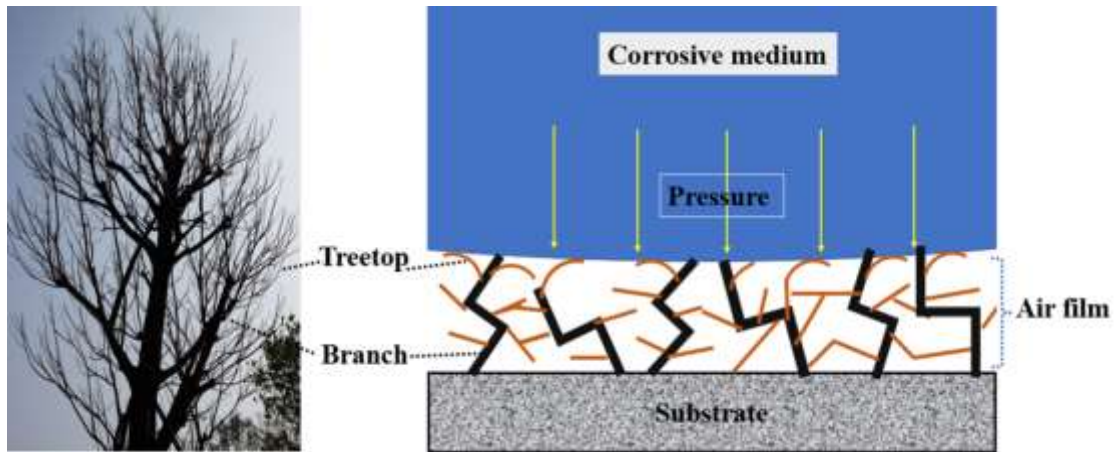
331 Figure 8a, 8b displayed Nyquist and Bode plots of 2.5EPZF specimens after  
332 different time's immersion in the NaCl solution (3.5 wt.%). The lowest impedance was  
333 related to the 2.5EPZF-35d sample. Nyquist plots for all 2.5EPZF samples with  
334 different time immersion consisted of two semi-circles. One semi-circle of the  
335 composite coating was related to coating properties in the high-frequency range and  
336 another one was attributed to double layers characteristics in the low-frequency range.

337 The Z view software was utilized for corresponding equivalent electrical circuits  
338 (Figure 8c). The circuits had various elements such as solution resistance ( $R_s$ ),  
339 charge-transfer resistance ( $R_p$ ), double layer constant phase element (CPE<sub>dl</sub>), pore  
340 resistance ( $R_c$ ), and coating constant phase element (CPE<sub>c</sub>). The highest value of  
341 composite coating resistance was related to 2.5EPZF-25d sample ( $1003 \Omega\text{cm}^2$ ). The  
342 lowest value of CPE<sub>p</sub> has also corresponded to 2.5EPZF-25d sample ( $3.008 \times 10^{-10}$ ).  
343 After 35 days' immersion the impedance of 2.5EPZF-35d sample decreased to below  
344 the impedance of 2.5EPZF-0d. It could be owed to the marvelous barrier property of

345 the superhydrophobic three-dimensional porous structure and after 35 days' immersion  
346 the corrosive media was partially wetted the 2.5EPZF coating.

### 347 *3.6. Protection mechanism for 2.5EPZF composite coating*

348 Figure 9 was the schematic representation of the Load-bearing corrosion protection  
349 mechanism for 2.5EPZF composite coating. The three-dimensional structure of  
350 2.5EPZF composite coating was like the Branch and Treetop. As shown in Figure 1 f,  
351 the 0.1-0.4  $\mu\text{m}$  mesh and 1-3  $\mu\text{m}$  skeleton of 2.5EPZF sample played the role as the  
352 Branch and Treetop of the tree, respectively. Under the pressure of the outside force  
353 (pressure of the corrosive medium), the deformation of treetop occurs and the pores of  
354 mesh and skeleton coating become denser to grasp the air film firmly. Furthermore, the  
355 1-3  $\mu\text{m}$  Branch structure of the 2.5EPZF coating provided the sufficient support to  
356 maintain the integrity of the air film. Then the Load-bearing type 2.5EPZF composite  
357 coating could afford more durable protection from corrosive media in the case of  
358 thinner coating.



359  
 360 **Figure. 9.** Schematic representation of the Load-bearing type corrosion protection mechanism for 2.5EPZF  
 361 composite coating.

362 *3.7. FT-IR spectra of PCL, PZ, PZF and 2.5EPZF coating&mechanical adhesion and*  
 363 *self-cleaning tests*

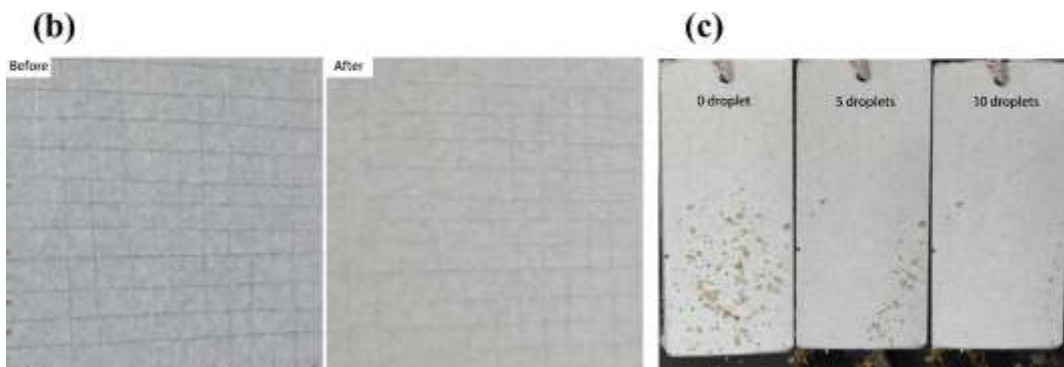
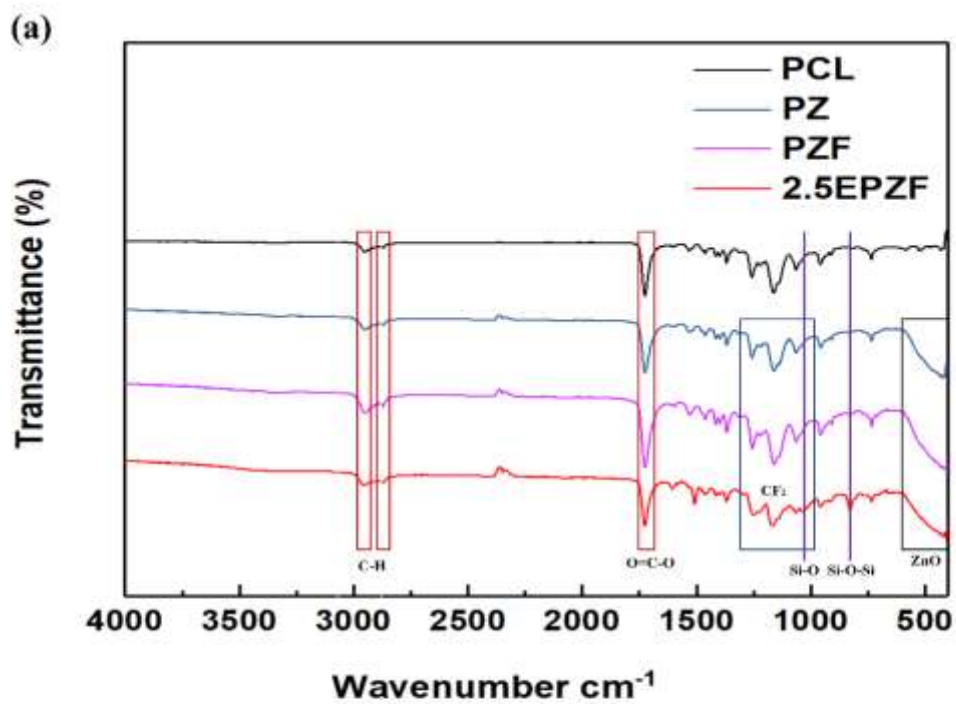
364 The FT-IR spectra of PCL, PZ, PZF and 2.5EPZF coating&mechanical adhesion and  
 365 self-cleaning tests were shown in Figure 10. The specific functional groups for PCL,  
 366 PZ, PZF and 2.5EPZF coating were evaluated by FTIR absorbance as shown in Figure  
 367 10a. The bands observed at  $2960-2870\text{ cm}^{-1}$  and  $1725\text{ cm}^{-1}$  were related to tensile  
 368 vibrations of C-H and Stretching vibrations of the ester carbonyl group, respectively  
 369 [51, 52]. Furthermore, bands at  $1462\text{ cm}^{-1}$  and  $1066\text{ cm}^{-1}$  were related to C-C and C-H  
 370 tension [46]. It was determined that the perceptible signal at  $400-600\text{ cm}^{-1}$  increased  
 371 with the addition of ZnO. The reason was that the ZnO material had an intense IR band  
 372 centered at  $442\text{ cm}^{-1}$  in the spectral region  $0-600\text{ cm}^{-1}$  [53]. The absorption bands  
 373 appearing at  $1300\text{ cm}^{-1} - 1000\text{ cm}^{-1}$  was attributed to the stretching mode of  $\text{CF}_2$  [54].

374 With the addition of PDFTES, the peaks between  $1300\text{ cm}^{-1}$  -  $1000\text{ cm}^{-1}$  increased.  
375 During solidification of the coating, EP and its cross-linker formed a net, and the  
376 PDFTES would move towards the surface during the coat's solidification because the  
377 PDFTES was highly hydrophobic and the EP system was hydrophilic [46]. The  
378 characteristic absorption peaks of Si-O and O-Si-O appeared at  $1035\text{ cm}^{-1}$  and  $827\text{ cm}^{-1}$ ,  
379 which illustrated that the amount of PDFTES on the surface of 2.5EPZF sample  
380 significantly increased [55]. It indicated that PDFTES had transferred to the surface of  
381 the composite coating with solidification of EP.

382 Generally, the stability of adhesive materials on the surface is one of the main  
383 challenges of coating [56,57]. The adhesion strength between coating and magnesium  
384 alloy was evaluated according to ASTM D3359-09 method [49]. The result of adhesion  
385 measurement illustrated that the 2.5EPZF coating in Figure 10b showed very few  
386 flakes detached at intersections. It suggested that the bonding strength between the  
387 2.5EPZF coating and magnesium sample was strong enough to be potentially used in  
388 physiological environments.

389 Lotus-inspired superhydrophobic surface features self-cleaning effect [58]. The  
390 self-cleaning ability of 2.5EPZF coating was evaluated and displayed in Figure 10c.

391 Due to the SA being less than  $10^\circ$ , water droplets could slide on the surface of the  
 392 2.5EPZF sample easily. And the self-cleaning test was measured to evaluate the  
 393 self-cleaning ability of the 2.5EPZF coating as shown in Figure 10c. The self-cleaning  
 394 test result illustrated that the sand on the surface of the 2.5EPZF sample was carried  
 395 away mostly after 10 water droplets, which proved that the composite coating was with  
 396 good self-cleaning performance.

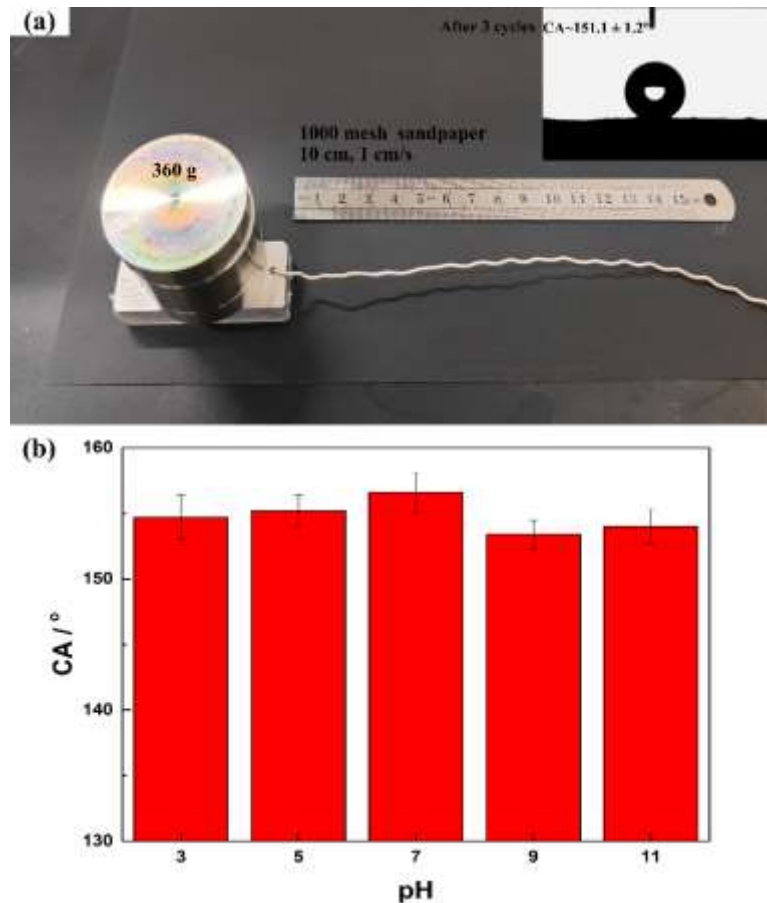


397  
 398 **Figure 10.** FTIR analysis of PCL, PZ, PZF and 2.5EPZF coating (a), the results of mechanical adhesion  
 399 (b) and self-cleaning test (c).

400 3.8. *Abrasion resistance and pH stability test*

401 Figure 11 showed the results of abrasion resistance test and pH durability of  
402 2.5EPZF coating. The mechanical abrasion resistance of 2.5EPZF was measured by the  
403 sandpaper abrasion test to evaluate the tribological properties [59, 60]. The result of  
404 the 2.5EPZF coating's sandpaper abrasion experiment was as shown in Figure 11a. The  
405 2.5EPZF coating was abraded on a 1000-mesh sandpaper under a weight of 360.0 g at a  
406 constant speed of 1 cm/s. After 3 cycles of total length of 30 cm, the CA of 2.5EPZF  
407 coating was  $151.1 \pm 1.2^\circ$  with a small amount of debris falling.

408 The contact angle test of the water droplets with different pH values was carried out  
409 on the surface of the 2.5EPZF coating to determine the resistance of the coating to acid  
410 and alkali solutions. As shown in Figure 9b, the CA of the 2.5EPZF coating surface  
411 increased first and then decreased with the increase of pH value, but it is higher than  
412  $153^\circ$ . The results indicated that the 2.5EPZF coating had excellent chemical stability.



413

414 **Figure. 11.** The mechanical abrasion resistance (a) and pH durability (b) of 2.5EPZF coating.

### 415 3.9. *Bacillus subtilis* adhesion test and corrosion resistance test

416 Figure 12 showed the results of *Bacillus subtilis* adhesion test for 20 days at 30 °C

417 and 120 pm and corrosion resistance test in 3.5% wt NaCl at room temperature. In

418 experiment, three parallel samples from each group. After the bacterial adhesion test,

419 the tested samples were fixed in 2.5% glutaraldehyde aqueous solutions for 20 minutes.

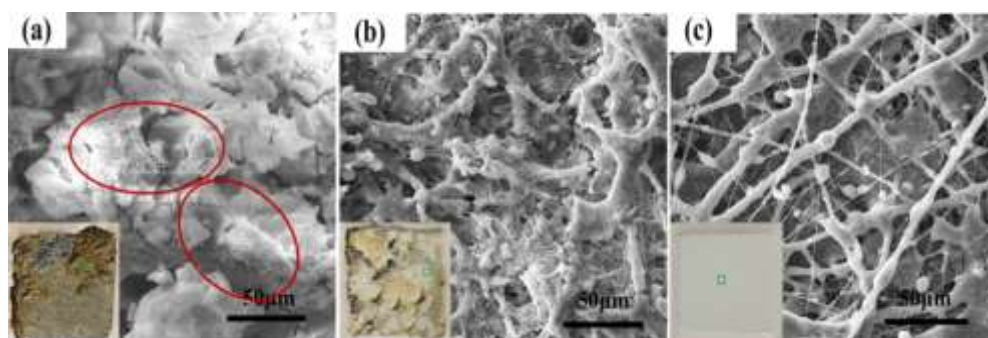
420 Then divided them into ethanol solution at 5%, 15%, 25%, 45%, 65%, 85%, 95% of the

421 step concentration in proper order. In the end, dehydrated in anhydrous ethanol for 20

422 minutes and dried for natural air. Figure 12a, b and c showed the digital photos and

423 SEM images of magnesium alloy substrate, PZF and 2.5EPZF samples after 20 days in  
424 Bacillus culture. Figure 12a, 12b and 12c were the digital photos and SEM images of  
425 magnesium alloy substrate, PZF and 2.5EPZF samples after the Bacillus subtilis  
426 adhesion test. There was the serious corrosion of the AZ91D magnesium  
427 alloy substrate as the Digital photo shown. Furthermore, there were many bacilli on the  
428 corrosion surface of magnesium alloy as shown in SEM image of Figure 12a. It showed  
429 that AZ91D magnesium alloy was prone to corrosion and microbial attachment in the  
430 marine environment containing  $\text{Cl}^-$  and marine bacteria (Bacillus). There were the  
431 perceptible coating damage and measurably bacillus adhesion of the magnesium  
432 substrate in the Bacillus environment for 20 days' immersion in Figure 10a. Compared  
433 with the magnesium alloy substrate, the PZF coating was damaged partially and the  
434 pitting pits were produced. It showed that the degradable PCL combined with PFDTES  
435 could not provide sufficient protection for magnesium alloy in the marine environment  
436 containing  $\text{Cl}^-$  and marine bacteria (Bacillus). In Figure 12b, the SEM image of some  
437 residual PZF coating illustrated that the PZF coating had a good anti-adhesion effect  
438 against Bacillus. Figure 12c was the digital photo and SEM image of the 2.5EPZF  
439 composite coating sample after 20 days' immersion in the Bacillus environment. The

440 results showed that the 2.5EPZF composite coating had no obvious surface damage and  
441 corrosion. The protective 2.5EPZF coating was still intact and the three-dimensional  
442 structure of the coating was also maintained. What's more, there was no obvious  
443 bacillus adhesion. It showed that 2.5EPZF composite coating could provide sufficient  
444 protection for magnesium alloy samples and had strong adhesion resistance to marine  
445 bacteria Bacillus.



446  
447 **Figure. 12.** Digital photos&SEM images of magnesium alloy substrate (a), PZF (b) and 2.5EPZF (c) samples  
448 after 20 days in Bacillus culture at 30°C: magnesium alloy substrate.

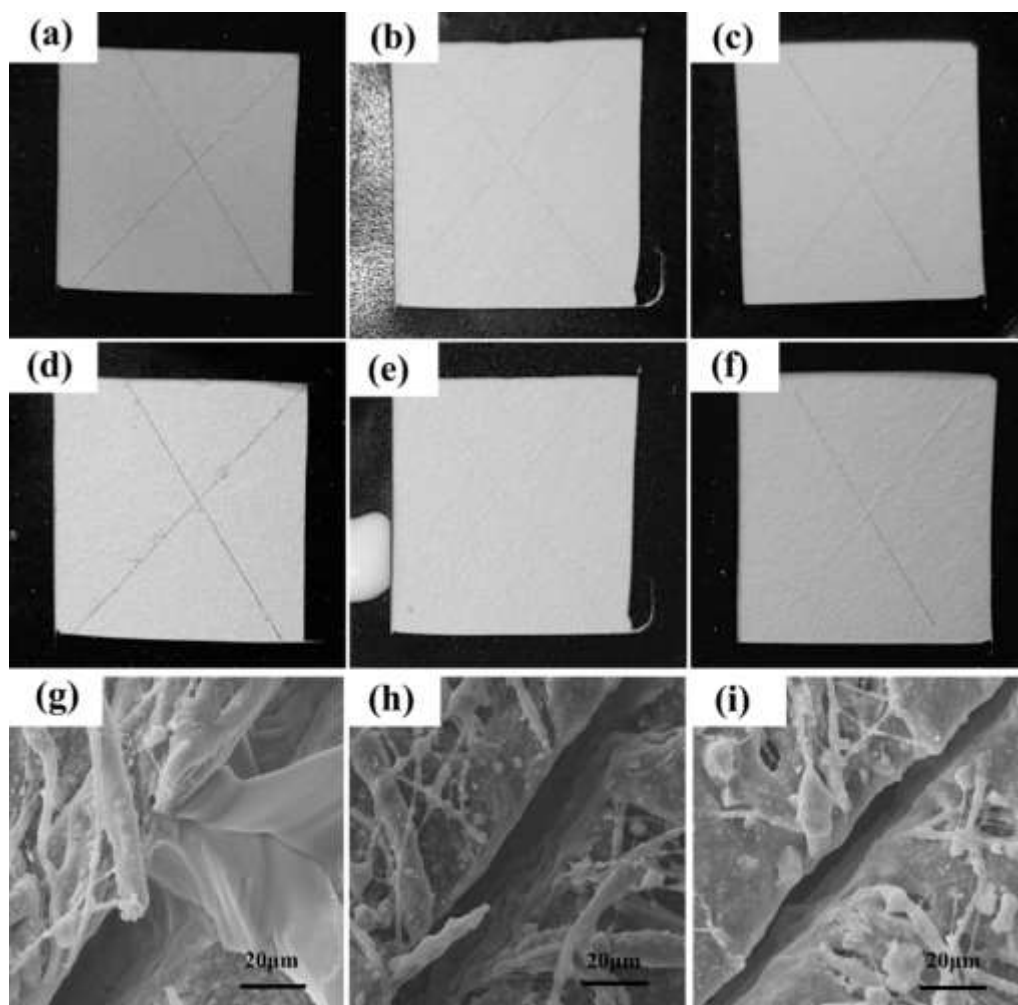
### 449 3.10. Solar irradiation and thermal repair, grid corrosion test

450 Drew a big cross on the surface of superhydrophobic 2.5EPZF composite coating  
451 with a surgical blade. The scratch depth exposed the magnesium alloy, and the scratch  
452 width was about 20-25 µm. A group of crossed 2.5EPZF composite coating samples  
453 were exposed to outdoor direct sunsolar irradiation for 6 hours (Wuhan, September).  
454 Another group of crossed 2.5EPZF composite coating was placed in an oven at 50 °C  
455 for 30 min, and then took out to the air and cooled to room temperature. The crossed

456 2.5EPZF samples without solar irradiation or heating were used as the control group.  
457 During the accelerated corrosion test of scratched 2.5EPZF samples, the above three  
458 groups of samples were placed in the 10% wt NaCl solutions at 30 °C for 24 hours.  
459 After that, took them out to the outdoor environment for 20 days to observe the surface  
460 changes of the samples (as shown in Figure 13). The 2.5EPZF samples before (Figure  
461 13a) and after (Figure 13d) grid corrosion test and the SEM image (Figure 13g)  
462 illustrated that the 2.5 EPZF composite coating could provide protection for  
463 magnesium alloy matrix, and only corrosive medium infiltration occurs at the scratch.  
464 The 2.5EPZF samples under 6 hours' solar irradiation before (Figure 13b), after  
465 (Figure 13e) grid corrosion test and the 2.5EPZF samples at 50 °C for 30min before  
466 (Figure 13c), after (Figure 13f) grid corrosion test showed that there was no corrosive  
467 medium infiltration at the scratch. It showed that 2.5EPZF sample would be repaired to  
468 a certain extent after sunsolar irradiation or at 50 °C for 30 min to prevent the  
469 corrosion damage of corrosion medium NaCl to the sample.

470 The EDS data (Table 4) showed that the content of Si and F of 2.5EPZF coating  
471 increased significantly after illumination and heating at 50 °C. Under the solar  
472 irradiation or heating at 50 °C, the PFDTES on the coating surface would undergo a

473 certain amount of molecular transfer and the redistribution of perfluorinated branched  
 474 chains, which would repair the scratch gap to a certain extent, increase the  
 475 hydrophobicity, reduce the invasion of corrosive media, and improve the corrosion  
 476 protection ability of scratches.



477  
 478 **Figure. 13.** Digital photos scratched 2.5EPZF samples before&after grid corrosion test, 2.5EPZF samples at 50  
 479 °C for 30 min before (c)&after (f) grid corrosion test and the SEM of sample of scratched 2.5EPZF after  
 480 accelerated corrosion test; 2.5EPZF samples before (a)&after (d) grid corrosion test; 2.5EPZF samples under  
 481 solar irradiation before (b) and after (e) grid corrosion test; 2.5EPZF samples at 50 °C for 30 min before (c) and  
 482 after (f) grid corrosion test and the SEM of sample of scratched 2.5EPZF after accelerated corrosion test;  
 483 2.5EPZF samples under solar irradiation before (b) and after (e) grid corrosion test; 2.5EPZF samples at 50 °C  
 484 for 30 min before (c) and after (f) grid corrosion test.

Samples	C/ wt%	O/ wt%	Zn/ wt%	F/ wt%	Si/ wt%
---------	--------	--------	---------	--------	---------

2.5EPZF	60.0	18.6	16.7	4.4	0.3
2.5EPZF after sunsolar irradiation	54.6	22.3	17.9	4.8	0.4
2.5EPZF at 50°C for 30min	55.0	21.9	17.4	5.2	0.5

485 **Table 4.** The EDS of samples with 2.5EPZF composite coating.

486 *3.11. The large scale&irregular shape preparation of 2.5EPZF coating and their*  
487 *superhydrophobicity*

488 The preparation of the large scale&irregular shape with the superhydrophobic  
489 2.5EPZF coating was shown in Figure 14. In Figure 14a, the results illustrated that the  
490 spraying method to prepare the 2.5EPZF coating could complete the large area  
491 preparation and the composite 2.5EPZF coating was with the superhydrophobicity of  
492 ink, juice, milk and tea. Figure 14b indicated that the preparation of superhydrophobic  
493 coating could be assisted in rapid application to irregularly shaped substrate.



494 **Figure. 14.** Digital photos of the large scale&irregular shape samples with 2.5EPZF coating and their  
495 superhydrophobicity: (a) large scale samples with 2.5EPZF coating and the superhydrophobicity of ink,  
496 juice, milk and tea; (b) irregular shape samples with 2.5EPZF coating and the superhydrophobicity of water 2.5EPZF  
497 samples.

#### 499 **4. Conclusions**

500 In this study, by one-step spray method a three-dimensional superhydrophobic  
501 2.5EPZF composite coating was prepared. The spraying method provides a feasible  
502 solution to prepare the controllable three-dimensional structure coating. The 2.5EPZF  
503 composite coating has durable hydrophobic, good mechanical adhesion and  
504 self-cleaning, antifouling and corrosion resistance. The composite coating also has the  
505 function of repairing scratches under sunsolar irradiation and heating at 50 °C.  
506 Furthermore, the superhydrophobic large scale&irregular shape of 2.5EPZF composite  
507 coating can be prepared. The above functions have application value for the  
508 application of 2.5EPZF composite coating in marine ships.

### 509 **Declaration of Competing Interest**

510 The authors declare that they have no known competing financial interests or  
511 personal relationships that could have appeared to influence the work reported in this  
512 paper.

### 513 **Acknowledgment**

514 We gratefully acknowledge financial support from the Innovation and Development Joint Fund  
515 Key Project of Hubei Provincial Natural Science Foundation (2022CFD029).

### 516 **References**

517 [1] M.S. Joun, S.M. Ji, J.D. Yoo, S.H. Chung, H.K. Moon, E.J. Kim, D.J. Yoon, J.M. Choi, A.  
518 Babu, Characterization of AZ31B, AZ61A and AZ80A magnesium alloys with an emphasis on  
519 temperature compensation for their application to a hot forging. *J. Manuf. Process.* 84 (2022)  
520 764-785, <https://doi.org/10.1016/j.jmapro.2022.10.054>.

521 [2] X.D. Chen, Q.Z. Cai, Z.W. Deng, L.S. Yin, Research and Application of Micro-Arc Oxidation  
522 Technology on Magnesium Alloy Motorcycle Key Parts. *Appl. Mechan. Mater.* 496-500 (2014)  
523 63-70, <https://doi.org/10.4028/www.scientific.net/amm.496-500.63>.

524 [3] S. Chen, J. Zhang, Y. Chen, S. Zhao, M. Chen, X. Li, F.M Manfred, J. Wang, N. Huang,  
525 Application Of Phenol/Amine Copolymerized Film Modified Magnesium Alloys: Anticorrosion  
526 And Surface Biofunctionalization. *ACS Appl. Mater. Interfaces.* 7 (2015) 24510-24522,  
527 <https://doi.org/10.1021/acsami.5b05851>.

528 [4] G. Wang, J.P. Weiler, Recent developments in high-pressure die-cast magnesium alloys for  
529 automotive and future applications, *J. Magnes. Alloy.* 11 (2023) 78-87.

530 [5] J. Moreno, J.L. Merlo, A.C. Renno, J. Canizo, F.J. Buchelly, J.I. Pastore, M.R. Katunar, S.  
531 Cere, In vitro characterization of anodized magnesium alloy as a potential biodegradable material  
532 for biomedical applications, *Electrochim. Acta.* 437 (2023) 141463,  
533 <https://doi.org/10.1016/j.electacta.2022.141463>.

534 [6] M. Ahmadi, S.A.A.B Tabary, D. Rahmatabadi, M.S. Ebrahimi, K. Abrinia, R. Hashemi,  
535 Review of selective laser melting of magnesium alloys: advantages, microstructure and  
536 mechanical characterizations, defects, challenges, and applications, *J. Mater. Re. Technol.* 19  
537 (2022) 1537-1562, <https://doi.org/10.1016/j.jmrt.2022.05.102>.

538 [7] P. Karuppusamy, K. Lingadurai, V. Sivananth, S. Arulkumar, A study on mechanical properties  
539 of tungsten carbide reinforced magnesium metal matrix composites for the application of piston,  
540 *Int. J. Solar irradiationweight Mater. Manuf.* 4 (2021) 449-459,  
541 <https://doi.org/10.1016/j.ijlmm.2021.06.007>.

542 [8] J.M. Seitz, R. Eifler, M. Vaughan, C. Seal, M. Hyland, H.J. Maier, Coating Systems for  
543 Biodegradable Magnesium Applications, *Magnes. Technol.* 2014, pp. 371-374.

544 [9] H. Hu, A. Yu, N. Li, J.E. Allison, Potential Magnesium Alloys for High Temperature Die Cast  
545 Automotive Applications: A Review. *Mater. Manuf. Process.* 18 (2003) 687-717,  
546 <https://doi.org/10.1081/AMP-120024970>.

547 [10] A.M. Zhang, P. Lenin, R.C. Zeng, M.B. Kannan, Advances in hydroxyapatite coatings on  
548 biodegradable magnesium and its alloys, *J. Magnes. Alloy.* 10 (2022) 1154-1170,  
549 <https://doi.org/10.1016/j.jma.2022.01.001>.

550 [11] X. He, J. Liu, C. Yang, G. Jiang, Predicting thermodynamic stability of magnesium alloys in  
551 machine learning, *Comp. Mater. Sci.* 223 (2023) 112111,  
552 <https://doi.org/10.1016/j.commatsci.2023.112111>.

553 [12] J. Jiang, Y. Wang, Y. Li, W. Shan, S. Luo, Microstructure and mechanical properties of the  
554 motorcycle cylinder body of AM60B magnesium alloy formed by combining die casting and  
555 forging, *Mater. Design.* 37 (2012) 202-210, <https://doi.org/10.1016/j.matdes.2012.01.012>.

556 [13] Y.K. Gao, D.W. Gao, Y.H. Gao, A Study on Magnesium Alloy Substitution Design and  
557 Analysis for Automotive Seat Back Frame, *Adv. Mater. Res.* 156-157 (2010) 245-251,  
558 <https://doi.org/10.4028/www.scientific.net/AMR.156-157.245>.

559 [14] A. Kielbus, T. Rzychoń, R. Cibis, Microstructure of AM50 die casting magnesium alloy. *J.*  
560 *Achiev. Mater. Manuf. Eng.* 18 (2006) 135-138.

561 [15] H. Friedrich, S. Schumann, Research for a “new age of magnesium” in the automotive  
562 industry, *J. Mater. Proc. Technol.* 117 (2001) 276-281,  
563 [https://doi.org/10.1016/S0924-0136\(01\)00780-4](https://doi.org/10.1016/S0924-0136(01)00780-4).

564 [16] C. Suman, The Effects of Direct Aging on Mechanical Properties and Corrosion Resistance of  
565 Diecast Magnesium Alloys AZ91D and AM60BN, SAE Technical Paper 900794, SAE  
566 February-March, 1990.

567 [17] A. Kiebus, M. SozaĚska, L. Cizek, Microstructural characterization of AZ91 magnesium  
568 alloy, *Magnesium Alloys and Their Applications*, Wolfsburg. 2003. pp. 190-195.

569 [18] X. Jia, J. Song, B. Xiao, Q. Liu, H. Zhao, Z. Yang, J. Liao, L. Wu, B. Jiang, A. Atrens, F. Pan,  
570 Influence of indentation size on the corrosion behaviour of a phosphate conversion coated AZ80  
571 magnesium alloy, *J. Mater. Res. Technol.* 14 (2021) 1739-1753,  
572 <https://doi.org/10.1016/j.jmrt.2021.07.091>.

573 [19] J. Ouyang, Y. Gao, Dense nanoarrays LDHs film evenly dividing the Cl<sup>-</sup> diffusion path into  
574 longitudinal microchannels in favor of quasi-uniform corrosion of biomedical magnesium alloys,  
575 *Surf. Coat. Tech.* 449 (2022) 128981, <https://doi.org/10.1016/j.surfcoat.2022.128981>.

576 [20] F. Ge, Z. Cui, Y. Liu, L. Lei, X. Wang, H. Cui, Influence of ammonium sulfate on the  
577 corrosion behavior of AZ31 magnesium alloy in chloride environment, *J. Magnes. Alloy.* xxx  
578 (xxxx) xxx, <https://doi.org/10.1016/j.jma.2022.07.014>.

579 [21] B. Vaghefinazari, S.V. Lamaka, C. Blawert, M. Serdechnova, N. Scharnagl, P. Karlova, D.C.F.  
580 Wieland, M.L. Zheludkevich, Exploring the corrosion inhibition mechanism of  
581 8-hydroxyquinoline for a PEO-coated magnesium alloy. *Corros. Sci.* 203 (2022) 110344,  
582 <https://doi.org/10.1016/j.corsci.2022.110344>.

583 [22] S.M. Ganji, M. Tehranchi, A. Ehterami, H. Semyari, F. Taleghani, M. Habibzadeh, M.H.  
584 Tayeed, N. Mehrnia, A. Karimi, M. Salehi, Bone tissue engineering via application of a

585 PCL/Gelatin/Nanoclay/Hesperetin 3D nanocomposite scaffold, *J. Drug Deliv. Sci. Tec.* 76 (2022)  
586 103704, <https://doi.org/10.1016/j.jddst.2022.103704>.

587 [23] Q.Z. Yuan, C. Shi, T.S. He, Design and performance optimization of self-cleaning coating on  
588 decorative UHPC surface, *Constr. Build. Mater.* 394 (2023) 132115,  
589 <https://doi.org/10.1016/j.conbuildmat.2023.132115>.

590 [24] J. Lv, C.X. Zhu, H.N. Qiu, J. Zhang, C.D. Gu, J. Feng, Robust icephobic epoxy coating using  
591 maleic anhydride as a crosslinking agent, *Prog. Org. Coat.* 142 (2020) 105,  
592 <https://doi.org/10.1016/j.porgcoat.2020.105561>.

593 [25] X.Q. Fan, S.J. Song, Y.T. Shi, M. Cai, Y. Huang, B.B. Zhang, M.H. Zhu, Mechanochemical  
594 stable superhydrophobic coating toward lasting corrosion protection, *Prog. Org. Coat.* 178 (2023)  
595 107478, <https://doi.org/10.1016/j.porgcoat.2023.107478>.

596 [26] Z.X. Yang, L.C. Jing, X.B. Ming, W.H. Geng, W.W. Cao, Y.H. Tian, P.S. Bin, Z.L. Bao, R.Y.  
597 Chang, H.Z. Geng, Preparation and performance study of superhydrophobic layer based on fluffy  
598 ZnO rods/PDMS, *Surf. Interfaces.* 39 (2023) 102968,  
599 <https://doi.org/10.1016/j.surfin.2023.102968>.

600 [27] G.H. Zhang, P.P. Wang, X.X. Zhang, C.H. Xiang, L.L. Li, The preparation of PCL/MSO/SiO<sub>2</sub>  
601 hierarchical superhydrophobic mats for oil-water separation by one-step method, *Euro. Polym. J.*  
602 116 (2019) 386-3, <https://doi.org/10.1016/j.eurpolymj.2019.04.011>.

603 [28] Z.M. Jiang, B.T. D. Nguyen, J.H. Seo, C. Hong, D. Kim, S. Ryu, S. Lee, G. Lee, Y. H. Cho,  
604 J.F. Kim, K. Lee, Superhydrophobic polydimethylsiloxane dip-coated polycaprolactone  
605 electrospun membrane for extracorporeal membrane oxygenation, *J. Membrane. Sci.* 679 (2023)  
606 121715, <https://doi.org/10.1016/j.memsci.2023.121715>.

607 [29] P. Cao, H. Wang, L.M. Zhao, Y.R. Zhou, J. Zhang, Y.Y. Zhang, L.X. Zheng, Q.W. Li, Robust,  
608 amphiphobic and super-buoyant CNT foams promising for self-floating functional platforms,  
609 *Carbon.* 168 (2020)439-447, <https://doi.org/10.1016/j.carbon.2020.06.037>.

610 [30] X.B. Zhang, Y.P. Hu, W. Yang, M.B. Feng, Ag-loaded and Pd-loaded ZnO nanofiber  
611 membranes: preparation via electrospinning and application in photocatalytic antibacterial and  
612 dye degradation, *Appl. Nanosci.* 13 (2023) 1495-1506,  
613 <https://doi.org/10.1007/s13204-021-02056-3>.

614 [31] D.F. Arisoy, W.K. Kolewe, B. Homyak, S.I. Kurtz, D.J. Schiffman, J.J. Watkins, Bioinspired  
615 Photocatalytic Shark-Skin Surfaces with Antibacterial and Antifouling Activity via Nanoimprint  
616 Lithography. *ACS Appl. Mater. Inter.* 23(2018)20055-20063,  
617 <https://doi.org/10.1021/acsami.8b05066>.

618 [32] S.D. Zhi, G. Wang, Z.X. Zeng, L.J. Zhu, Z.X. Liu, D.W. Zhang, K.L. Xu, Q.J. Xue, 3D mossy  
619 structures of zinc filaments: A facile strategy for superamphiphobic surface design, *J. Colloid*  
620 *Interf. Sci.* 526 (2018) 106-113, <https://doi.org/10.1016/j.jcis.2018.04.083>.

621 [33] K.M. Lee, H. Park, J. Kim, D.M. Chun, Fabrication of a superhydrophobic surface using a  
622 fused deposition modeling (FDM) 3D printer with poly lactic acid (PLA) filament and dip coating  
623 with silica nanoparticles, *Appl. Surf. Sci.* 467-468 (2019) 979-991,  
624 <https://doi.org/10.1016/j.apsusc.2018.10.205>.

625 [34] M. Amin, M. Singh, K.R. Ravi, Fabrication of superhydrophobic PLA surfaces by tailoring  
626 FDM 3D Printing and chemical etching process, *Appl. Surf. Sci.* (2023) 157217,  
627 <https://doi.org/10.1016/j.apsusc.2023.157217>.

628 [35] S. Rathinavel, P.S. Korrapati, P. Kalaiselvi, S. Dharmalingam. Mesoporous silica  
629 incorporated PCL/Curcumin nanofiber for wound healing application, *Eur. J. Pharm. Sci.* 167  
630 (2021) 106021, <https://doi.org/10.1016/j.ejps.2021.106021>.

631 [36] J. Hu, B. Yang, F. Jin, P. Soo-Jin, Fracture toughness and surface morphology of  
632 polysulfone-modified epoxy resin. *J. Ind. Eng. Chem.* 25 (2015) 9-11,  
633 <https://doi.org/10.1016/j.jiec.2014.10.032>.

634 [37] M.Y. Li, Z.H. Min, Q.C. Wang, W. Huang, Z.Y. Shi, Effect of epoxy resin content and  
635 conversion rate on the compatibility and component distribution of epoxy asphalt: A MD  
636 simulation study, *Constr. Build. Mater.* 319 (2022) 126050,  
637 <https://doi.org/10.1016/j.conbuildmat.2021.126050>.

638 [38] F. Ferdosian, Y.S. Zhang, Z.S. Yuan, M. Anderson, C. Xu, Curing kinetics and mechanical  
639 properties of bio-based epoxy composites comprising lignin-based epoxy resins, *Eur. Polym. J.* 82  
640 (2016) 153-165, <https://doi.org/10.1016/j.eurpolymj.2016.07.014>.

641 [39] S.R. Ravi, J.P. Girish, B. Vivek, I.K. Muhammad, E. Nouredine, S. Abdallah, L. Rafael, An  
642 eco-friendly approach on green synthesis, bio-engineering applications, and future outlook of ZnO  
643 nanomaterial: A critical review, *Environ. Res.* 221 (2023) 114807,  
644 <https://doi.org/10.1016/j.envres.2022.114807>.

645 [40] B. Baro, S. Khimhun, U. Das, S. Bayan, ZnO based triboelectric nanogenerator on textile  
646 platform for wearable sweat sensing application, *Nano Energy.* 108 (2023) 108212,  
647 <https://doi.org/10.1016/j.nanoen.2023.108212>.

648 [41] Y.L. Zhang, Y.L. Zhang, Y. Lei, J.R. Wu, Y.Y. Kang, S. Zheng, L.Q. Shao, MDM2  
649 upregulation induces mitophagy deficiency via Mic60 ubiquitination in fetal microglial  
650 inflammation and consequently neuronal DNA damage caused by exposure to ZnO-NPs during  
651 pregnancy, *J. Hazard. Mater.* (2023) 131750, <https://doi.org/10.1016/j.jhazmat.2023.131750>.

652 [42] Y.J. Zheng, K.L. Wang, L. Sun, H.L. Shi, X. Zhang, Preparation of PFDTs-kaolin/PU  
653 superamphiphobic coatings with antibacterial, antifouling and improved durability property, *Prog.*  
654 *Org. Coat.* 173 (2022) 107145, <https://doi.org/10.1016/j.porgcoat.2022.107145>.

655 [43] P. Cao, H. Wang, L.M. Zhao, Y.R. Zhou, J. Zhang, Y.Y. Zhang, L.X. Zheng, Q.W. Li, Robust,  
656 amphiphobic and super-buoyant CNT foams promising for self-floating functional platforms,  
657 *Carbon.* 168 (2020)439-447, <https://doi.org/10.1016/j.carbon.2020.06.037>.

658 [44] B. Saha, W.Q. Toh, E. Liu, S.B. Tor, J. Lee, A study on frictional behavior of PMMA against  
659 FDTs coated silicon as a function of load, velocity and temperature, *Tribol. Int.* 102 (2016) 44-51,  
660 <https://doi.org/10.1016/j.triboint.2016.04.018>.

661 [45] P.Z. Wang, L. Zhang, Z.Q. Hu, J.Q. Shang, J. Zhou, Transparent and anti-fingerprint coating  
662 prepared with chitin nanofibers and surface modification via vapor deposition, *Prog. Org. Coat.*  
663 172 (2022) 107126, <https://doi.org/10.1016/j.porgcoat.2022.107126>.

664 [46] J. Zhang, W.C. Zhang, J.J. Lu, C.X. Zhu, W.Q. Lin, J. Feng, Aqueous epoxy-based  
665 superhydrophobic coatings: Fabrication and stability in water, *Prog. Org. Coat.* 121 (2018) 201-2,  
666 <https://doi.org/10.1016/j.porgcoat.2018.04.012>.

667 [47] S.K. Sethi, S. Kadian, R. Gogoi, G. Manik, Layer-by-layer fabrication of self-cleaning  
668 superhydrophobic surface made from Carboxymethylcellulose and ZnO quantum dots: A combined  
669 experimental and computational study, *Surf. Interfaces.* 37 (2023) 102752,  
670 <https://doi.org/10.1016/j.surfin.2023.102752>.

671 [48] L.L. Xie, J.H. Chu, X.J. Li, D.N. Zou, L.B. Tong, Improved corrosion resistance of EP  
672 coating on Mg alloy through GO hybridization and silica-based superhydrophobic surface, *Diam.*  
673 *Relat. Mater.* 130 (2022) 109476, <https://doi.org/10.1016/j.diamond.2022.109476>.

674 [49] Z.X. Xi, C. Tan, L. Xu, Y.Z. Meng, C.Y. Zhang, N. Yang, Q. Li, A novel functional  
675 HPPS/PCL/ZnO composite layer on AZ91 for anticorrosion, *Mater. Lett.* 148 (2015) 134-137,  
676 <https://doi.org/10.1016/j.matlet.2015.02.056>.

677 [50] Y.H. Xie, X.F. Zhou, H.Y. Mi, J.H. Ma, J.Y. Yang, J. Cheng, High efficiency ZnO-based  
678 dye-sensitized solar cells with a 1H,1H,2H,2H-perfluorodecyltriethoxysilane chain barrier for  
679 cutting on interfacial recombination, *Appl. Surf. Sci.* 434 (2018) 1144-1152,  
680 <https://doi.org/10.1016/j.apsusc.2017.11.075>.

681 [51] M.A.J. Kouhbanani, S. Mosleh-Shirazi, N. Beheshtkhoo, S. R. Kasaei, S. Nekouian, S.  
682 Alshehry, H. Kamyab, S. Chelliapan, M. Azam Ali, A.M. Amani, Investigation through the  
683 antimicrobial activity of electrospun PCL nanofiber mats with green synthesized Ag-Fe  
684 nanoparticles, *J. Drug. Deliv. Sci. Tec.* 85 (2023) 104541,  
685 <https://doi.org/10.1016/j.jddst.2023.104541>.

686 [52] M. K k, M.E. Pekdemir, E. .  ner, M. C. kun, S. Hekim, MWCNT nanocomposite films  
687 prepared using different ratios of PVC/PCL: Combined FT-IR/DFT, thermal and shape memory  
688 properties, *J. Mol. Struct.* 1279 (2023) 134989, <https://doi.org/10.1016/j.molstruc.2023.134989>.  
689 [53] X.Y. Li, A.X. Lu, H.M. Yang, Structure of ZnO-Fe<sub>2</sub>O<sub>3</sub>-P<sub>2</sub>O<sub>5</sub> glasses probed by Raman and IR  
690 spectroscopy, *J. Non-Cryst. Solids.* 389 (2014) 2-27,  
691 <http://dx.doi.org/10.1016/j.jnoncrsol.2014.01.051>.  
692 [54] H.F. Yang, C.H. Xu, W.M. Wang, P.F. Tang, X.D. Li, S.S. He, H.B. Bao, S.S. Man, D.Y. Tang,  
693 X.M. Li, G.C. Yang, Z.Q. Qiao, Underwater self-sustaining combustion and micro-propulsion  
694 properties of Al@FAS-17/PTFE-based direct-writing nanothermite, *Chem. Eng. J.* 451 (2023)  
695 138720, <https://doi.org/10.1016/j.cej.2022.138720>.  
696 [55] S.L. Chen, M. Yang, Y.Y. Han, H.D. Liu, H.T. Zou, Hydrophobically modified sustainable  
697 bio-based polyurethane for controllable release of coated urea, *Euro. Polym. J.* 142 (2021) 110114,  
698 <https://doi.org/10.1016/j.eurpolymj.2020.110114>.  
699 [56] J.C. Ma, Y.Q. Qing, H.Y. Song, X.J. Cheng, Z.R. Li, C. Long, C.S. Liu, Synergistically  
700 coupled double conductive coating-based electronic textiles with superhydrophobic and  
701 high-performance strain sensing properties for underwater human motion sensing applications,  
702 *Chem. Eng. J.* 471 (2023) 144284, <https://doi.org/10.1016/j.cej.2023.144284>.  
703 [57] C.L. Li, Cai Long, Y. Cai, Z.H. Li, Z.Y. Guan, H.Y. Song, L. Guo, X.Y. Xu, C.S. Liu, Y.Q.  
704 Qing, Design of amphoteric micro/nanofiber-coupling fabric for ultrafast, precise, and robust  
705 removal of water droplets from oils, *Chem. Eng. J.* 471 (2023) 144479,  
706 <https://doi.org/10.1016/j.cej.2023.144479>  
707 [58] T. Shi, H.N. Wang, Q. Jia, R.Y. Chen, Preparation of a transparent coating with  
708 superamphiphobic and antifouling properties, *Mater. Chem. Phys.* 293 (2023) 126888,  
709 <https://doi.org/10.1016/j.matchemphys.2022.126888>,  
710 [59] Z.L. Wang, A.B. Yang, X.Y. Tan, Y.T. Tu, S. Sabin, P. Xiang, M. Wang, R.H. Guo, X.B. Chen,  
711 A veil-over-sprout micro-nano PMMA/SiO<sub>2</sub> superhydrophobic coating with impressive abrasion,  
712 icing, and corrosion resistance, *Colloids. Surface. A.* 601 (2020) 1249,  
713 <https://doi.org/10.1016/j.colsurfa.2020.124998>.  
714 [60] Y.X. Bai, H.P. Zhang, J. Zhu, Y.Y. Shao, H. Zhang, A durable superhydrophobic coating based  
715 on inherent nano/micro-integrated materials, *Prog. Org. Coat.* 184 (2023) 107854,  
716 <https://doi.org/10.1016/j.porgcoat.2023.107854>.